Nano World Journal

https://doi.org/10.17756/nwj.2023-s1-024

Research Article

Open Access

Mechanical Performance of Additive Manufactured PEEK Composite

Vipin Gupta[1], N. I. Thiruselvam [1*], D.M. Kulkarni[1], V.V. Chaudhari[1] and S. Suraj[2]

[1]Birla Institute of Technology and Science Pilani, K.K. Birla Goa Campus, Zuarinagar, Goa, India

[2]Vikram Sarabhai Space Centre, Thiruvananthapuram, Kerala, India

[*]Correspondence to:
Iniyan N Thiruselvam
Birla Institute of Technology and Science Pilani, K.K. Birla Goa Campus, Zuarinagar, Goa, India.
E-mail: iniyann@goa.bits-pilani.ac.in

Received: November 24, 2022
Accepted: April 01, 2023
Published: April 03, 2023

Citation: Gupta V, Thiruselvam NI, Kulkarni DM, Chaudhari VV, Suraj S. 2023. Mechanical Performance of Additive Manufactured PEEK Composite. *NanoWorld J* 9(S1): S119-S124.

Published by United Scientific Group

Abstract

Carbon-reinforced polyether ether ketone or C-PEEK has many uses in engineering applications. Fused Deposition Modeling (FDM) is the additive manufacturing method of choice for producing C-PEEK components because of its low cost and high efficiency. Anisotropy is commonly associated with such components because of the raster angle between the printing and loading directions. However, the impact of raster angle on the local state of strain has received comparatively less focus. The present work attempts to fill this research gap using Digital Image Correlation (DIC) to measure full-field deformation of C-PEEK. Standard specimens are tested for failure by fracture at 0°, 45°, and 90° raster angles. The strength is the highest at 0° raster angle, whereas it is the lowest at 90° raster angle. Brittle fracture is the cause of failure for all samples. The most important part of the failure mechanism is played by strain localization that develops near the interfaces between adjacent beads or layers.

Keywords

Fused deposition modeling, Carbon-reinforced PEEK, Digital image correlation, Scanning electron microscope

Introduction

Polyether ether ketone (PEEK) is widely used in space applications because it is a semi-crystalline high-performance thermoplastic polymer with a high strength-to-weight ratio, appealing thermo-mechanical properties, and a low outgassing index [1-3]. Due to its biocompatibility, radiolucency, chemical resistance, low density, and low friction coefficient [4-5], it is also used in biomedical applications such as orthopedic and dental implants. Submarines and offshore structures made of PEEK can operate at depths of up to 6,000 meters [6]. To improve the physical, thermal, and chemical properties of PEEK, reinforcements such as nanoparticles, thin sheets, laminates, fibers, and fabrics are used. Among the several reinforcements reported in the literature, carbon fiber is the most commonly used one [3, 7, 8]. The resulting composite material is referred to as C-PEEK in the present work. C-PEEK is superior to PEEK polymer in terms of strength and thermal expansion coefficient [9, 10]. The manufacturing processes of C-PEEK manufacturing can be broadly classified as follows.

- Subtractive (e.g., machining, cutting, milling, and grinding),
- Formative (e.g., pressing, casting, forming, injection moulding, and polymer extrusion), and
- Additive (e.g., 3D printing).

Subtractive manufacturing involves the removal of excess material to create a final product. Formative process used tooling such as various molds, dies, fixtures,

patterns, and other devices to create a product. It is impossible to make a design change without investing in new tools for the subtractive and formative processes. As a result, the higher level of design complexity increases production costs. On the other hand, prototypes, models, and finished parts with complex geometries can be made using additive manufacturing (AM) technologies without requiring specialized equipment. In this method, the material is deposited onto a substrate in a series of layers until the final product matches the specifications of the design drawing [11]. AM results in a 30 - 40% reduction in raw material usage compared to traditional fabrication methods [12, 13].

Due to its low cost, ease of operation, negligible wastage of material, and high efficiency [14], FDM has gained popularity in fabricating products made of thermoplastic polymer among the AM technologies. A filament is continuously fed through motor-driven wheels to the melting head, where it is heated to its melting temperature. The filament is heated to between 100 - 250 °C, fed through a nozzle, and deposited in layers onto a build platform. Printing parameters like raster width, raster angle, bead overlap percentage, layer height, build orientation, nozzle temperature, bed temperature, and chamber temperature affect the mechanical properties of FDM C-PEEK products. When examining the effect of these variables on the mechanical behavior of FDM C-PEEK, raster angle was found to have the highest impact [7-9, 13-17]. The highest strength was achieved at a 0° raster angle than the others [16, 18-21]. However, it is found that literature lacks in-depth investigation in this area, particularly one that uses full-field deformation measurement with Digital Image Correlation (DIC) [22, 23] to resolve the local state of strain at high resolution.

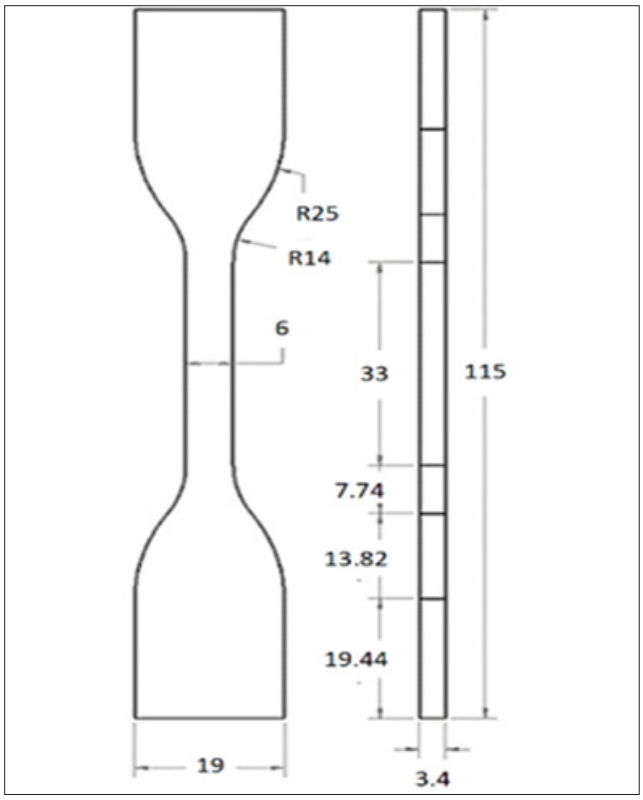

Figure 1: Specimen dimensions.

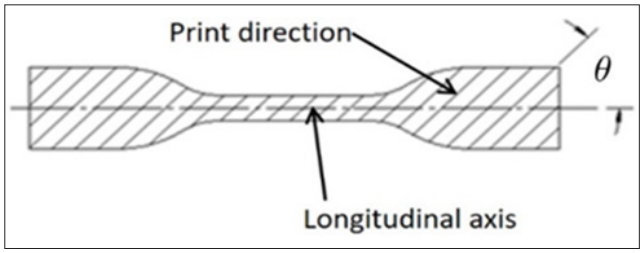

Figure 2: Raster angle (θ) between the print direction and the longitudinal axis (tensile axis) of the test specimen.

In this work, we analyze the deformation of FDM C-PEEK during a uniaxial tensile test using in-house 2D-DIC software. Each step is performed by following recently published good practices guidelines (GPG) for DIC [24]. Tensile deformations of test specimens printed at 0°, 45°, and 90° are compared by analyzing their tensile strength, percentage of elongation, modulus of elasticity, and the spatial distribution of equivalent von Mises strains obtained with DIC. Scanning electron microscopy (SEM) secondary electron images are used to examine the fractured surfaces. In this work, DIC and SEM analyses are used to shed light on the raster angle dependence of the anisotropy and the deformation heterogeneity of FDM C-PEEK.

Materials and Methods

Fused deposition modeling

Commercially available KetaSpire® PEEK AM filament CF10 LS1 (Solvay S.A., Brussels, Belgium) was fed into a HYDRA 16AS FDM 3D Printer to create C-PEEK dog-bone specimens (ASTM D638 standard) (AMS HYREL, Ban-galore, India). The diameter of the filament is 1.75 mm, and its density is 1.33 g/cm^3. The printer has an X and Y positioning accuracy of 60 µm and a Z positioning accuracy of 10 µm. Figure 1 depicts the test specimen's dimensions. Figure 2 shows raster angle between the print direction and the longitudinal axis of the test specimen.

To ensure that there was no interlayer gap or raster gap on any of the surfaces of the manufactured specimens, they were examined under a microscope. Each of the three sets, S1 (0°), S2 (45°), and S3 (90°), is comprised of four good specimens. They were prepared to conduct uniaxial tensile tests. Table 1

Table 1: parameters (excluding raster angle) of FDM C-PEEK dog-bone specimens.

Parameter	Value
Layer Thickness (mm)	0.2
Printing Speed (mm/s)	20
Nozzle Temperature (°C)	390
Bed Temperature (°C)	120
Infill (%)	100
Nozzle diameter (mm)	0.4
Number of contours (outlines)	2
Environment Temperature (°C)	55

shows the fixed printing parameters of FDM C-PEEK specimens.

Uniaxial tensile test and DIC setup

Each specimen was given a random speckle pattern on its surface by first painting it with a thin layer of white paint, then lightly misting it with black paint. Figure 3 depicts the experimental setup used in the current study. At room temperature (25 °C), tensile tests were conducted on specimens

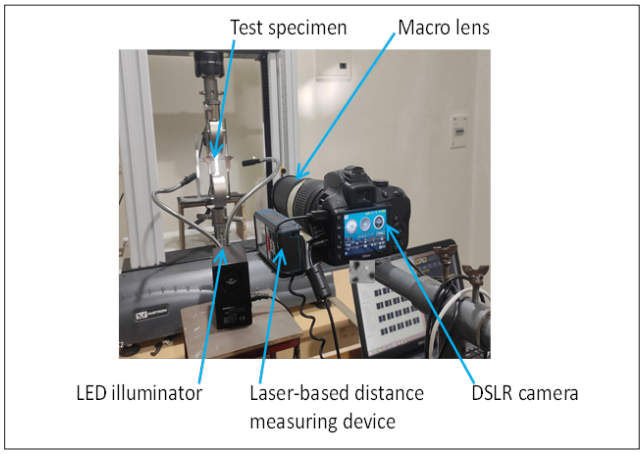

Figure 3: Experimental setup.

S1, S2, and S3 using the Instron Universal Testing Machine (50 kN, Norwood, MA, United States). These samples were tested with a 30 kN load cell at a displacement rate of 0.1 mm/min. The testing speed accuracy was set at 0.2% of the set speed. The force measurement accuracy of the machine is within 1%, and the positional accuracy is within ±20 µm. The grip-to-grip distance in each test was set to be 60 mm.

Specifically, the DIC system employed here consists of a Nikon D3300 camera (6000 × 8000 pixels, 3.87 µm pixel size) coupled with a Tamron 300 mm macro lens (Figure 3), with the magnification set to 1:2. Millimeter-scale specimen deformation studies are feasible with this setup. During the tests, the camera was placed in manual focus and care was taken to prevent any movement of the camera or lens. To prevent any unintentional shifting, the focus ring was firmly taped down. The exposure settings were 1/50 sec., f/25, and ISO 100.

Using a Bosch GLM 500 laser-based distance measuring device, we ensured that the lens was always perpendicular to the surface of the specimen and the ground (Robert Bosch GmbH, Ger-many). Each tensile test began with a verification of the planarity constraint between the specimen plane and the sensor plane. During the tensile tests, a 24 W LED illuminator was used to illuminate the test specimens, and the room's ambient light level was maintained at a constant 60 cd/m^2. We used a sturdy tripod stand and a camera with a rigid mount for this. Therefore, the imaging system was isolated from environmental vibrations.

Since the imaging system had a shallow depth of field, the camera had to be precisely positioned so that the entire specimen stayed in focus as it was deformed. The camera was timed to take a picture once every four seconds using ESPER Trigger Box (Esper Ltd., Nottingham, UK). The DIC was performed on the images collected until the point of fracture failure to measure the local state of strain.

DIC Optimization

Images collected during the tensile test were processed using our proprietary 2D-DIC algorithm. Lens distortion corrections were applied to the collected images first, using the method described in GPG [24]. For this reason, we calibrated the camera from various angles covering both the horizontal and vertical planes, as described in [25]. Finally, the displacement and strain maps for each deformation stage were computed using the DIC optimization fueled by a high-quality initial guess [26]. It is worth noting that DIC's output included strain information (i.e., the in-plane strain tensor) for each measurement node as defined by the undisturbed reference image.

As suggested by GPG [24], a virtual strain gauge (VSG) study is conducted. A subset size (SU), step size (ST), and strain window (SW) size were all independently investigated in the VSG study. In this VSG analysis, the following ranges of parameters are used: SU = (10, 15, 20, 25, 30, 35, and 40), ST = (1, 2, and 3), and SW = (2, 4, 6, 8, 10, 12, and 15). The optimal combination obtained from VSG study is used for DIC analysis. The formula used to find VSG is as follows.

$$VSG = [(SW - 1) \times ST] + SU \quad (1)$$

It was found that SU = 30 pixels, ST = 1 pixel, and SW = 2 pixels provided the best trade-off between bias and noise in the DIC strain measurements. The tensile deformation of the three sets of test specimens, S1 (0°), S2 (45°), and S3 (90°), were analyzed using the DIC results obtained. This analysis helps to explore the effect of the raster angle on the tensile behavior of FDM C-PEEK.

SEM Imaging

The geometry of deformation could be inferred from the fractured surface of the test specimens. Secondary electron images obtained from a SEM were used for conducting microstructure analyses of the fractured surface. Before testing, ethanol was used to clean the fractured surfaces of the test specimens. After that, Leica EM ACE200 sputtering machine was used to sputter coat each fractured surface (Leica Microsystems GmbH, Wetzlar, Germany). Argon gas was used to create plasma to sputter gold nanoparticles with a size distribution of 3 - 5 nm onto the fractured surface. It is to be noted that charging the specimen can cause noise or distortion in the images, which can be greatly reduced by sputtering gold nanoparticles. Finally, scanning electron microscopy (Quanta FEG 250, FEI, Lausanne, Switzerland) was used to collect images of the fractured surface at an accelerating voltage of 20 kV, a spot size level of 3.0, and a working distance of 8 - 10 mm. The fractured surfaces of S1, S2, and S3 specimens were compared using the obtained SEM images.

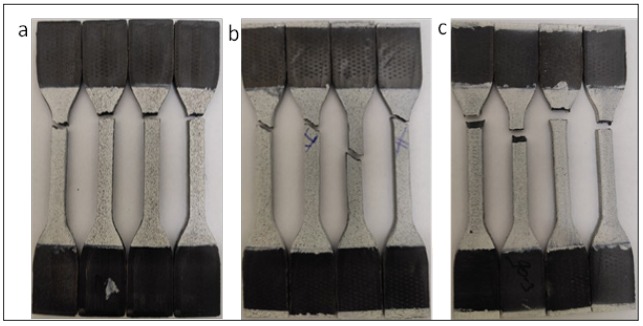

Figure 4: S1, S2, and S3, all of which failed by fracture, are shown in **(a)**, **(b)**, and **(c)**, respectively.

Results and Discussion

Tensile test results

Figure 4a, figure 4b, and figure 4c show the S1, S2, and S3 test specimens after deformation and failure by fracture, respectively. While all three samples exhibit brittle fractures, the resulting deformation geometry is distinct between them. Both S1 (Figure 4a) and S2 (Figure 4b) have fractured surfaces that are nearly perpendicular to the tensile axis (Figure 4b). S3 fractured surfaces are slanted at 30° to 60° to the thickness axis. For this reason, the behavior of each layer in S1 and S2 (along the thickness direction) is nearly identical.

In contrast, the deformation geometry at the onset of fracture is locally different in each layer of S3. These results suggest that the interlayer and inter-bead bonds in FDM C-PEEK play a crucial role in the material's failure mechanisms. It is worth noting that the SEM analysis results presented in the following subheading 3, confirm the same thing.

The Young's modulus (YM), ultimate tensile stress (UT), and percentage of elongation to failure (PE) are all calculated from the stress-strain curve for all four specimens in each set. Table 2 shows the average and standard deviation of the three material properties. The raster angle is negatively correlated with the three material properties (YM, UT, and PE). While S2 and S3 share very similar YM and UT values, S1's YM and UT values really stand out. As the raster angle is increased, PE is seen to decrease in a linear fashion. Anisotropy in FDM C-PEEK is responsible for the observed non-linear decrease in YM as a function of raster angle. The YM will vary in the 0°, 45°, and 90° directions if a normal force is applied to the printing direction at different angles.

DIC results

The axial, lateral and shear strains designated as ε_{tt}, ε_{ss} and ε_{st}, respectively are used to compute the principal strains ε_I, ε_{II} and ε_{III}. It is to be noted that only in-plane strains are computed, and hence, $\varepsilon_{III} = 0$. From the principal strains, the equivalent von Mises strain (ε_V) is calculated using the following equation.

$$\varepsilon_V = \frac{2}{3\sqrt{2}}\sqrt{(\varepsilon_I - \varepsilon_{II})^2 + (\varepsilon_{II} - \varepsilon_{III})^2 + (\varepsilon_{III} - \varepsilon_{II})^2} \quad (2)$$

At each deformation stage, ε_V computed all the points of interest are contained in matrices. These data matrices are further plotted as strain maps in figure 5a to 5e to visualize the spatial distribution of ε_V in the specimen gauge area. Figure 5a and 5b show ε_V at an applied stress of 20 MPa and 40 MPa for the S1, S2 and S3 specimens. At these two levels of applied stress, S2 and S3 deform more significantly than S1. At 20 MPa engineering stress, the minimum and maximum ε_V are 0.04% and 0.40% respectively in S1, whereas they are 0.29% and 1.05% respectively in both S2 and S3. At 40 MPa engineering stress, the minimum and maximum ε_V are 0.12% and 0.69% respectively in S1, whereas they are 0.35% and 1.67% respectively in S2 and S3 (Figure 5a and 5b). It is also evident that the spatial distribution of ε_V is heterogeneous in all three sets of specimens. Even at the early stages of deformation (i.e., at an applied stress of 20 MPa), some points of interest in S2 and S3 deform more than the others due to the underlying material inhomogeneity (subheading 3).

Generally, S1 does not show strain localization at 20 MPa and 40 MPa stresses, whereas both S2 and S3 clearly show strain localization. The localized strain peaks at 20 MPa stress are also seen in strain maps computed at 40 MPa stress. At the neighborhood of these data points, the spatial distribution of strains remains qualitatively unchanged between these two stages of deformation (i.e., 20 MPa and 40 MPa) though there are changes in the strain magnitude between them. However, several new regions of strain localization appear in the latter stages of deformation. A more notable change in the distribution of localized strain peaks is seen between the S3 strain

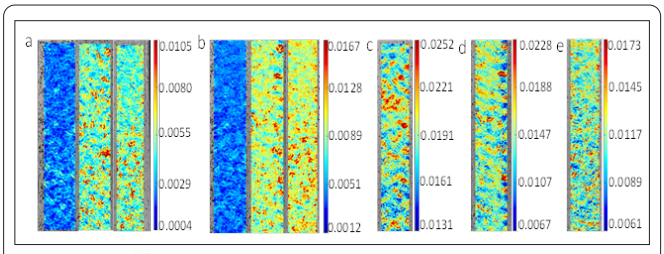

Figure 5: The ε_V strain maps at an applied stress of 20 MPa and 40 MPa are illustrated in **(a)** and **(b)** for the S1, S2 and S3 specimens. The strain maps at the ultimate tensile stress (UT) are plotted for S1, S2 and S3 in **(c)**, **(d)** and **(e)**, respectively.

Table 2: Young's modulus, ultimate tensile stress, and percentage of elongation till failure of the S1, S2, and S3 specimens.

Sample	Young's modulus (MPa)		Ultimate tensile stress (MPa)		Percentage of elongation (mm/mm)	
	Average	Standard Deviation	Average	Standard Deviation	Average	Standard Deviation
S1	9480.10	562.72	100.39	1.93	2.10	0.294
S2	4349.45	120.85	51.34	2.66	1.84	0.142
S3	4057.37	499.59	46.45	4.80	1.56	0.190

maps computed at 20 MPa and 40 MPa stresses (Figure 5a and 5b). These observations depict that the evolution of the strains over time is not the same for all the points of interest, i.e., some regions in the gauge area deform faster than the others. The spatial distribution of ε_V is clearly heterogeneous in all three sets of specimens (Figure 5c to 5e), which may be attributed to the material inhomogeneity that stems from the process used to fabricate the test specimens.

SEM Analysis

The microstructure analysis performed on the fractured surfaces of the failed test specimens confirms the findings of the DIC analyses. Surface morphology of fractures in S1, S2, and S3 is depicted in figure 6, micro defects like fibre pull-out, air pores, and interlayer gaps, as well as the mode of fracture, are examined to provide an overall assessment of the fractured surfaces. All FDM C-PEEK specimens break brittlely, as evidenced by the smooth fractured surfaces of S1, S2, and S3 samples. Bead-to-bead boundaries are not discernible in the fractured surface, whereas the layer boundary is clearly visible (Figure 6).

Compared to S2 and S3, the fibre density is higher in S1. The number of air gaps, the size of the air gaps, the orientation of the fibres in each layer, and the resulting geometry of deformation of each deposited layer all play a role in the variation in fibre distribution across the fractured surfaces. The number of air pockets are lowest in S1, followed by S2 and S3. Since most of the carbon fibres in S1 are oriented in the printing direction, they can withstand more pressure than S2 and S3. In S3, most of the fibres run perpendicular to the direction of loading. Additionally, in S3, the boundary between beads absorbs more stress than in S1 and S2. S3 has the lowest tensile strength of the three sets because the layer-to-layer bonding in PEEK polymer composites [17-23] is the weakest.

The bonding between beads and/or between layers is the most crucial factor in the failure mechanisms of FDM C-PEEK, as we saw in subheadings 1 and 2. At each deformation stage, the local state of strain is closest to the bead-to-bead interface. Both its scale and complexity are highly sensitive to the raster angle (Figure 5). Compared to S2 and S3, S1 exhibits more consistent deformation of the subsurface layers (Figure 6), which may be because 45° and 90° raster angles result in non-uniform plastic zones near each layer-to-layer interface. The observed heterogeneity and anisotropy in FDM C- PEEK stem from raster angle. In order to better understand the gradual change in material properties as a function of raster angle, further research along the same lines as the present work is needed. This would be accomplished through the use of high-resolution DIC and SEM with a wider range of raster angles.

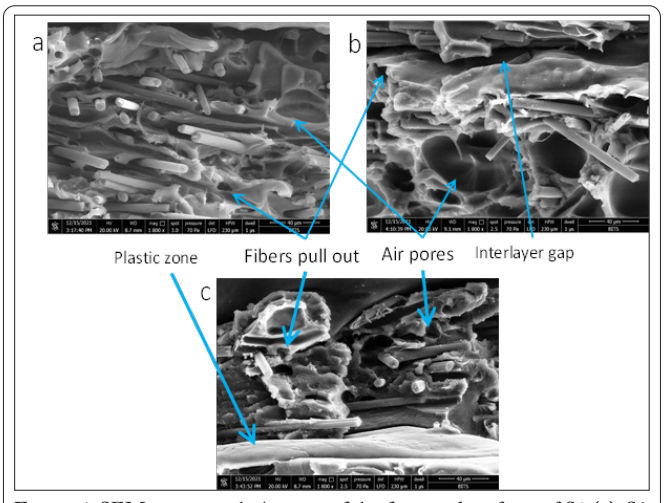

Figure 6: SEM micrographs/images of the fractured surfaces of S1 **(a)**, S2 **(b)**, and S3 **(c)** are illustrated.

Conclusions

C-PEEK was fabricated by FDM with three distinct print directions (raster angles), at 0°, 45°, and 90° with respect to the loading direction, and their anisotropy and deformation heterogeneity were investigated using high-resolution DIC and SEM. Anisotropy of FDM C-PEEK stems from raster angle. Tensile properties, including Young's modulus, ultimate tensile stress, and percent elongation to failure, show an inverse relationship to the raster angle. The strength is the highest at 0° raster angle, whereas it is the lowest at 90° raster angle. Strain heterogeneity of FDM C-PEEK is also a function of the raster angle. Strain data obtained via DIC shows spatial heterogeneity throughout the deformation process. Raster angle affects the local geometry of deformation close to the bead-to-bead and layer-to-layer boundaries. The most important part of the failure mechanism is played by strain localization that develops near the interfaces between adjacent beads or layers.

Acknowledgments

The authors would like to thank Indian Space Research Organization (ISRO) for funding this research work.

Conflict of Interest

None.

Credit Author Statement

Vipin Gupta: Conceptualization, Methodology, Formal analysis and Investigation, Writing – Original draft preparation, review and editing; N. I. Thiruselvam: Conceptualization, Methodology, Formal analysis and investigation, Writing – Original draft preparation, review and editing, Resources, Supervision; D. M. Kulkarni: Writing – review and editing, Resources, Supervision; V. V. Chaudhari: Writing – Original draft preparation, review and editing, Resources, Supervision; S. Suraj: Resources, Supervision.

References

1. Rival G, Dantras É, Paulmier T. 2022. Ageing of PEEK/Carbon Fibre composite under electronic irradiations: influence on mechanical behaviour and charge transport. *Compos A Appl Sci Manuf* 154: 106769. https://doi.org/10.1016/j.compositesa.2021.106769
2. Flanagan M, Grogan DM, Goggins J, Appel S, Doyle K, et al. 2017. Permeability of carbon fibre PEEK composites for cryogenic storage

tanks of future space launchers. *Compos A Appl Sci Manuf* 101: 173-184. https://doi.org/10.1016/j.compositesa.2017.06.013

3. Pastore R, Delfini A, Albano M, Vricella A, Marchetti M, et al. 2020. Outgassing effect in polymeric composites exposed to space environment thermal-vacuum conditions. *Acta Astronautica* 170: 466-471. https://doi.org/10.1016/j.actaastro.2020.02.019
4. Koh YG, Park KM, Lee JA, Nam JH, Lee HY, et al. 2019. Total knee arthroplasty application of polyetheretherketone and carbon-fiber-reinforced polyetheretherketone: a review. *Mater Sci Eng C* 100: 70-81. https://doi.org/10.1016/j.msec.2019.02.082
5. Han X, Yang D, Yang C, Spintzyk S, Scheideler L, et al. 2019. Carbon fiber reinforced PEEK composites based on 3D-printing technology for orthopedic and dental applications. *J Clin Med* 8(2): 240. https://doi.org/10.3390/jcm8020240
6. Davies P, Riou L, Mazeas F, Warnier P. 2005. Thermoplastic composite cylinders for underwater applications. *J Thermoplast Compos Mater* 18(5): 417-443. https://doi.org/10.1177/0892705705054397
7. Yasin S, Shakeel A, Ahmad M, Ahmad A, Iqbal T. 2019. Physico-chemical analysis of semi-crystalline PEEK in aliphatic and aromatic solvents. *Soft Mater* 17(2): 143-149. https://doi.org/10.1080/1539445X.2019.1572622
8. Russo P, Langella A, Leone G, D'Angelo G, Ferraro P, et al. 2021. Mechanical and morphological characterization of 3D-printed carbon PEEK composite for avionic shimming. In IEEE 8th International Workshop on Metrology for AeroSpace (MetroAeroSpace), pp 205-209. https://doi.org/10.1109/MetroAeroSpace51421.2021.9511708
9. Goyal RK, Tiwari AN, Mulik UP, Negi YS. 2007. Novel high performance Al_2O_3/poly (ether ether ketone) nanocomposites for electronics applications. *Compos Sci* Technol 67(9): 1802-1812. https://doi.org/10.1016/j.compscitech.2006.10.020
10. Hu B, Xing Z, Wu W, Zhang X, Zhou H, et al. 2021. Enhancing the mechanical properties of SCF/PEEK composites in FDM via process-parameter optimization. *High Perform Polym* 33(8): 914-923. https://doi.org/10.1177/09540083211003654
11. Gao W, Zhang Y, Ramanujan D, Ramani K, Chen Y, et al. 2015. The status, challenges, and future of additive manufacturing in engineering. *Comput Aided Des* 69: 65-89. https://doi.org/10.1016/j.cad.2015.04.0013
12. Martin-Iglesias P, van der Vorst M, Gumpinger J, Ghidini T. 2017. ESA's recent developments in the field of 3D-printed RF/microwave hardware. In IEEE 11th European Conference on Antennas and Propagation, pp 553-557. https://doi.org/10.23919/EuCAP.2017.7928852
13. Stepashkin AA, Chukov DI, Senatov FS, Salimon AI, Korsunsky AM, et al. 2018. 3D-printed PEEK-carbon fiber (CF) composites: structure and thermal properties. *Compos Sci Technol* 164: 319-326. https://doi.org/10.1016/j.compscitech.2018.05.032
14. Wong JY. 2016. 3D printing applications for space missions. *Aerosp Med Hum* Perform 87(6): 580-582. https://doi.org/10.3357/AMHP.4633.2016
15. Es-Said OS, Foyos J, Noorani R, Mendelson M, Marloth R, et al. 2000. Effect of layer orientation on mechanical properties of rapid prototyped samples. *Mater Manuf Process* 15(1): 107-122. https://doi.org/10.1080/10426910008912976
16. Abbasnezhad N, Khavandi A, Fitoussi J, Arabi H, Shirinbayan M, et al. 2018. Influence of loading conditions on the overall mechanical behavior of polyether-ether-ketone (PEEK). *Int J Fatigue* 109: 83-92. https://doi.org/10.1016/j.ijfatigue.2017.12.010
17. Algarni M, Ghazali S. 2021. Comparative study of the sensitivity of PLA, ABS, PEEK, and PETG's mechanical properties to FDM printing process parameters. *Crystals* 11(8): 995. https://doi.org/10.3390/cryst11080995
18. Sood AK, Ohdar RK, Mahapatra SS. 2010. Parametric appraisal of mechanical property of fused deposition modelling processed parts. *Mater Des* 31(1): 287-295. https://doi.org/10.1016/j.matdes.2009.06.016
19. Rahman KM, Letcher T, Reese R. 2015. Mechanical properties of additively manufactured PEEK components using fused filament fabrication. In ASME International Mechanical Engineering Congress and Exposition, Vol. 57359, pp V02AT02A009. https://doi.org/10.1115/IMECE2015-52209
20. Wu W, Geng P, Li G, Zhao D, Zhang H, et al. 2015. Influence of layer thickness and raster angle on the mechanical properties of 3D-printed PEEK and a comparative mechanical study between PEEK and ABS. *Materials* 8(9): 5834-5846. https://doi.org/10.3390/ma8095271
21. Pagliarulo V, Russo P, Leone G, D'Angelo GA, Ferraro P. 2022. A multimodal optical approach for investigating 3D-printed carbon PEEK composites. *Opt Lasers Eng* 151: 106888. https://doi.org/10.1016/j.optlaseng.2021.106888
22. Sutton MA, Orteu JJ, Schreier H. 2009. Image Correlation for Shape, Motion and Deformation Measurements: Basic Concepts, Theory and Applications. Springer, New York.
23. Blaber J, Adair B, Antoniou A. 2015. Ncorr: open-source 2D digital image correlation MATLAB software. *Exp Mech* 55(6): 1105-1122. https://doi.org/10.1007/s11340-015-0009-1
24. Jones EM, Iadicola MA. 2018. A Good Practices Guide for Digital Image Correlation. International Digital Image Correlation Society. https://doi.org/10.32720/idics/gpg.ed1/print.format
25. Thiruselvam NI, Subramanian SJ. 2020. On improving the accuracy of self-calibrated stereo digital image correlation system. *Meas Sci Technol* 32(2): 025201. https://doi.org/10.1088/1361-6501/abae3b
26. Thiruselvam NI, Subramanian SJ. 2019. Feature-assisted stereo correlation. *Strain* 55(5): e12315. https://doi.org/10.1111/str.12315